Vol. 33 (2002) *ACTA PHYSICA POLONICA B* No 10

QCD AND PROTON AND PHOTON STRUCTURE SINCE DIS2001*

J.J. Whitmore

U.S. National Science Foundation
and University of Pennsylvania, Philadelphia, PA 19104, USA

(Received August 12, 2002)

Results on proton and photon structure that have become available since the DIS2001 meeting are summarized.

PACS numbers: 13.85.Qk, 14.20.Dh, 14.70.Bh

1. Introduction

Each of the two HERA collider experiments, H1 and ZEUS, have now collected 16 pb^{-1} of e^-p data with a proton beam energy of 920 GeV and about 100 pb^{-1} of e^+p data with a proton energy of 820 or 920 GeV. The results presented here are given in terms of the usual Deep Inelastic Scattering (DIS) variables: s, the square of the ep center of mass energy; $Q^2 = -q^2$, the negative square of the four-momentum transfer of the virtual photon (essentially the "size" of the probing photon); $x = (Q^2/2p)q$, the fraction of the proton's momentum carried by the struck quark; and y, the inelasticity parameter. These variables are related by the expression $Q^2 = sxy$.

2. Measurements of the proton structure function, F_2

The kinematic region for DIS at HERA can be considered in three general areas. The transition region from photoproduction ($Q^2 \sim 0$) to the DIS region occurs near $Q^2 \sim 1$ GeV^2; $Q^2 > 4$ GeV^2 is the perturbative QCD (pQCD) region; and for $Q^2 > 10^4$ GeV^2, the electroweak (EW) sector overlaps with the Tevatron data and distances down to 1/1000th of the size of the proton are probed.

---

[*] Plenary presentation at the X International Workshop on Deep Inelastic Scattering (DIS2002) Cracow, Poland, 30 April–4 May, 2002.

2.1. Equations for cross sections

The cross sections for DIS can be expressed as

$$\frac{d\sigma_{e^\pm p}}{dxdQ^2} = \frac{2\pi\alpha^2}{xQ^4}\left(Y_+F_2 - y^2F_\mathrm{L} \mp Y_-xF_3\right) , \tag{1}$$

with $Y_\pm = 1 \pm (1-y)^2$. The structure function F_2^NC can be written as

$$F_2^\mathrm{NC} = x \sum_\mathrm{quarks} A_f\left(Q^2\right)\left[q\left(x,Q^2\right) + \bar{q}\left(x,Q^2\right)\right] . \tag{2}$$

F_L is the longitudinal structure function and the parity violating term xF_3^NC is sensitive only to valence quarks

$$xF_3^\mathrm{NC} = x \sum_\mathrm{quarks} B_f\left(Q^2\right)\left[q\left(x,Q^2\right) - \bar{q}\left(x,Q^2\right)\right] . \tag{3}$$

The reduced cross sections are defined as

$$\tilde{\sigma}_\mathrm{NC} = \frac{1}{Y_+}\frac{xQ^4}{2\pi\alpha^2}\frac{d^2\sigma}{dxdQ^2} , \tag{4}$$

and

$$\tilde{\sigma}_\mathrm{CC} = \frac{2\pi x}{G_F^2}\left(1 + \frac{Q^2}{M_W^2}\right)^2 \frac{d^2\sigma}{dxdQ^2} . \tag{5}$$

2.2. F_2 at HERA

The structure function F_2^{em} is shown as a function of x at fixed Q^2 [1] and as a function of Q^2 at fixed x [2] in Figs. 1 and 2, respectively.

The strong rise at low x is due to gluon radiation. The measurements from HERA now have a precision of about 3% (systematics) and match nicely with the fixed target data. The data exhibit strong scaling violations which may be seen more clearly in Figs. 3 and 4 [3].

The data can be well described by DGLAP QCD. Several groups (including H1, ZEUS, CTEQ and MRST) have performed Next-to-Leading-Order (NLO) QCD fits to the HERA and fixed target data. From these NLO fits to the measurements, both $\alpha_\mathrm{s}(M_Z^2)$ and the proton parton density functions (PDFs) may be determined. The H1 and ZEUS data and fits are in good agreement generally, but show differences at small values of x, see Fig. 2. The statistics are the limitation at large Q^2.

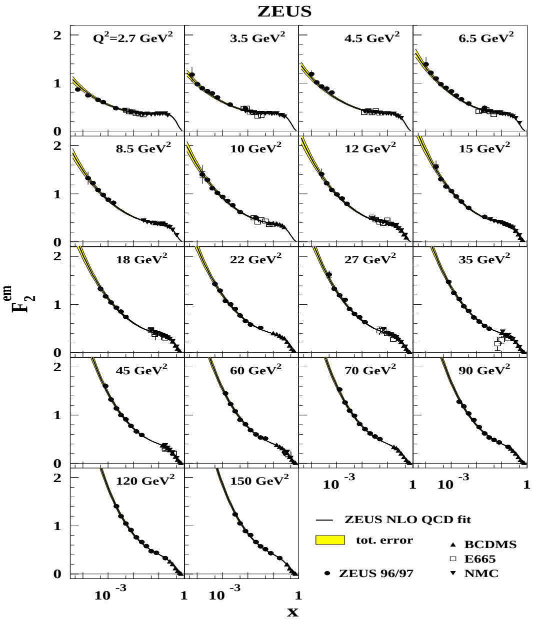

Fig. 1. The ZEUS NLO QCD fit compared to ZEUS 96/97 data and to fixed target data in low Q^2 bins.

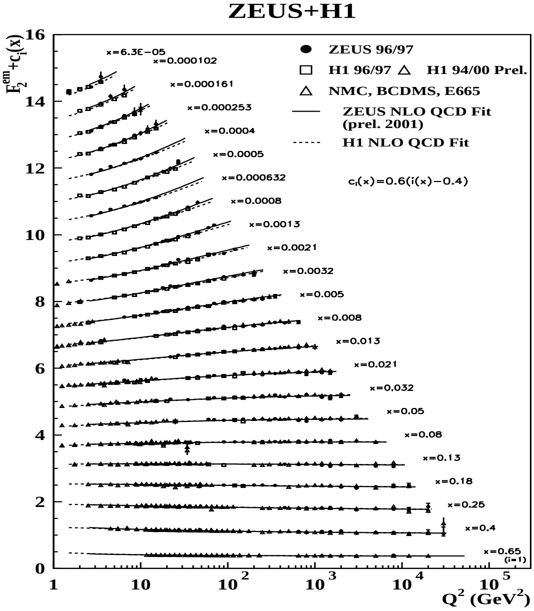

Fig. 2. The ZEUS and H1 NLO QCD fits compared to ZEUS 96/97 data, to H1 94/00 data and to fixed target data as a function of Q^2 at fixed x.

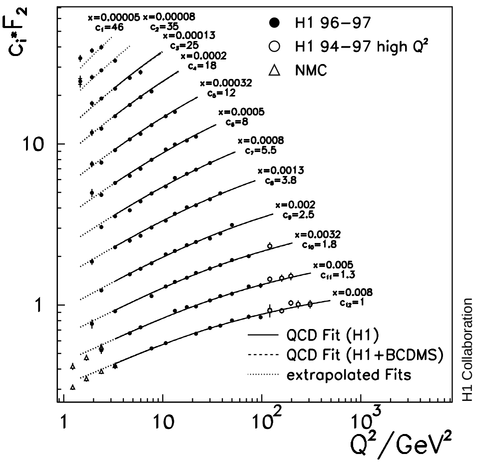

Fig. 3. Measurements of the proton structure function by H1 and the NMC experiments as a function of Q^2 at fixed x for $x < 0.01$. The solid curves are the NLO QCD fit by H1 to the H1 cross section data. The dashed curves are the results of the H1 fit to the H1 and NMC data.

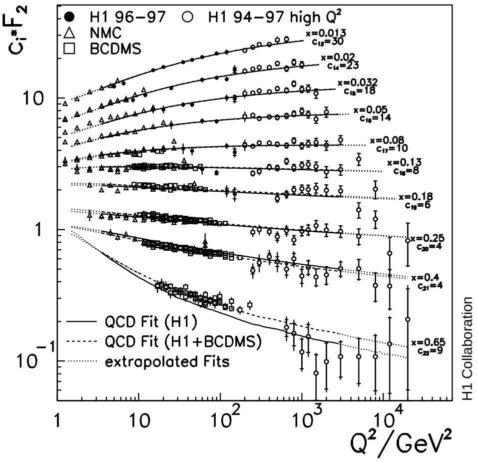

Fig. 4. As for Fig. 3, for higher x values, $x > 0.01$.

2.3. Proton PDFs

The gluon PDF, as obtained from H1 and ZEUS, is compared in Fig. 5 [2] where the evolution of the gluon is displayed. A comparison at the time of DIS2001 showed that there were some differences observed which are probably due to the heavy flavor scheme employed and to the parameterization of the gluon density. These differences will be discussed in talks by Tassi [4] and Reisert [5] at this workshop. The correlation with α_s is clearly visible

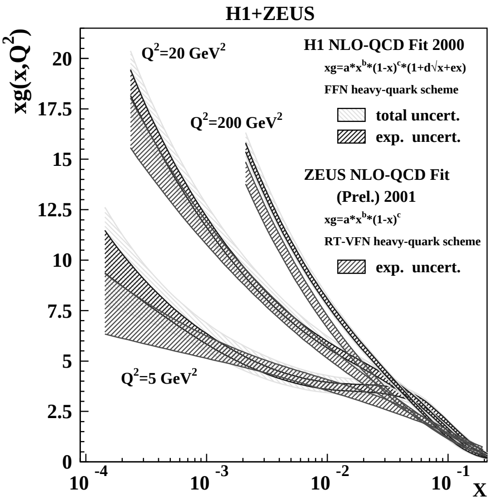

Fig. 5. A comparison of the gluon density as obtained by H1 and ZEUS as a function of x at three different Q^2 values.

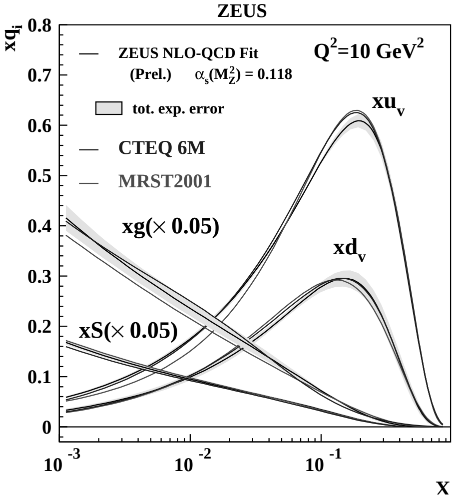

Fig. 6. A comparison of the proton PDFs as obtained by ZEUS with those from CTEQ6 and MRST2001 as a function of x at $Q^2 = 10$ GeV^2.

in the uncertainty on $xg(x)$. Fig. 6 shows [2] a comparison of the ZEUS PDFs with those from CTEQ6 and MRST2001. There is general agreement between all three within the uncertainties of the fitted PDFs, shown by the shaded lines for the ZEUS analysis.

2.4. Evaluation of the uncertainties in PDFs

Much work has gone into determining the uncertainties on the PDFs in order, for example, to estimate the uncertainties on predictions for parton luminosities at the LHC. In particular, the correlations between the experimental uncertainties have been taken into account by all PDF-fitting groups. The low-Q^2 and high-x regions have the largest uncertainties, as shown in Fig. 7 for the gluon [1] from ZEUS.

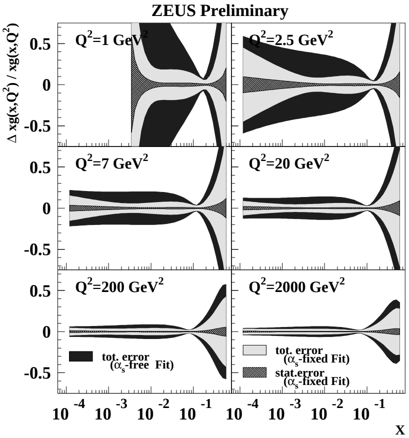

Fig. 7. The uncertainties on the gluon distribution from the standard ZEUS NLO QCD fit, shown as the ratio of the errors bands to the central value.

Fits have also been performed by ZEUS using either the standard set of data (which include the low energy, fixed target data) or using only ZEUS data, excluding the fixed target measurements but including the high Q^2 results from ZEUS. The resulting PDFs [2] are presented in Figs. 8 and 9.

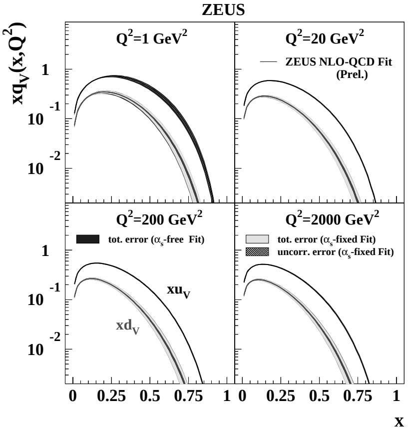

Fig. 8. The valence quark distributions obtained from the ZEUS NLO QCD fit to ZEUS and fixed target data (standard fit).

It can be seen that very similar results are obtained, indicating that the HERA data alone can constrain the PDFs at all x values.

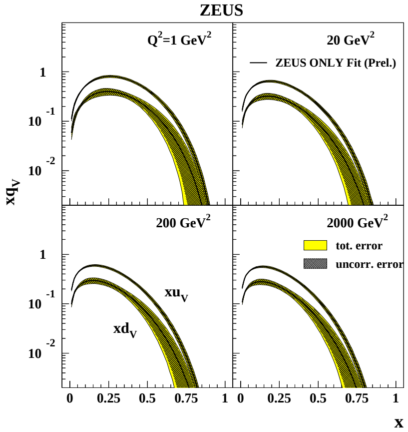

Fig. 9. The valence quark distributions obtained from the ZEUS NLO QCD fit to ZEUS data only.

2.5. Fits to the Tevatron high-$E_{\rm T}$ jet data

The new PDFs from CTEQ6 now describe the Tevatron high-$E_{\rm T}$ jet data quite well. This is shown in Figs. 10 and 11 which compare the D0 and CDF measurements with the CTEQ6M fits [6]. The improvement in the fits can be seen in Figs. 12 and 13 that display the ratio of data to theory for both CTEQ6 and CTEQ5 [6], respectively. The main difference in the two fits is a harder gluon distribution. This is in agreement with the ZEUS results, as was shown in Fig. 6.

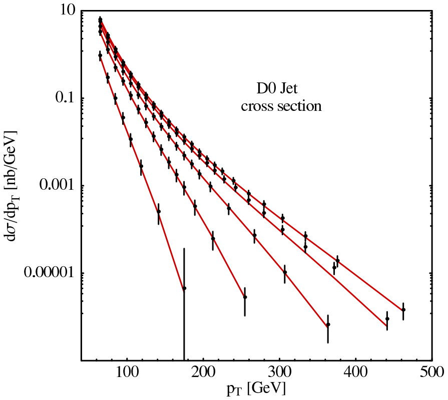

Fig. 10. Comparison of the CTEQ6M fit to the inclusive jet data from D0. The boundary values of the five rapidity bins are: 0, 0.5, 1.0, 1.5, 2.0 and 3.0.

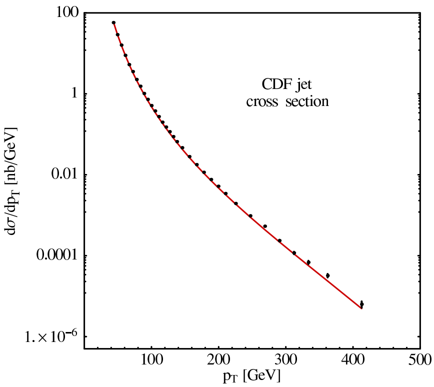

Fig. 11. Comparison of the CTEQ6M fit to the inclusive jet data from CDF, central rapidity $\eta < 0.5$.

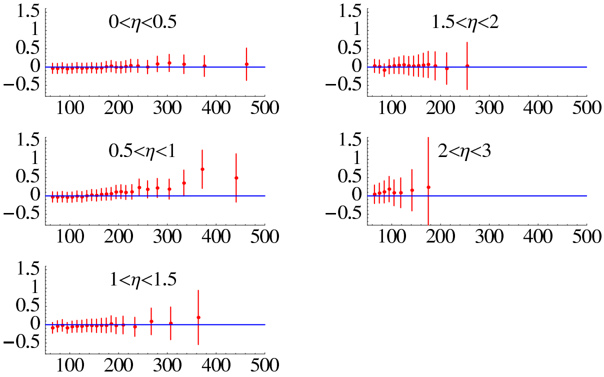

Fig. 12. A closer comparison between CTEQ6M and the D0 jet data. The plots show the ratio of (data-theory)/theory versus P_T in GeV.

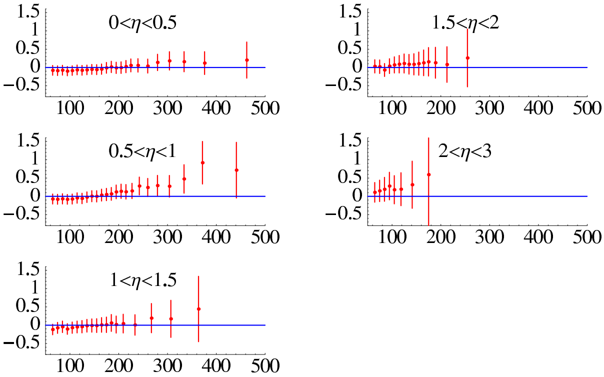

Fig. 13. As for Fig. 12, but compared to the CTEQ5M1 fits.

2.6. Range of validity for DGLAP evolution

The range of applicability of DGLAP evolution at low Q^2 has also been examined. Fig. 14 compares the ZEUS NLO fit using data with $Q^2 > 2.5\,\mathrm{GeV}^2$, evolved backwards to lower Q^2, with the ZEUS data at low Q^2 which were not used in the fit [1]. Clearly, the fit does not describe the data for Q^2 below ~1.5 GeV^2.

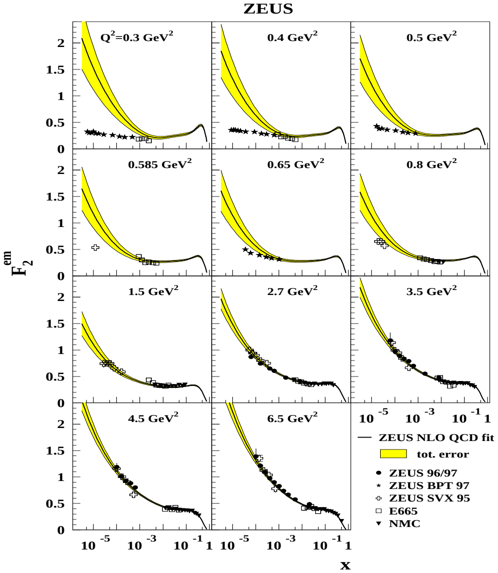

Fig. 14. F_2 data down to very low Q^2 compared to the standard ZEUS NLO QCD fit backward extrapolated.

2.7. DIS cross sections at high Q^2

The cross sections at high Q^2 have been measured by both H1 and ZEUS for both the Neutral Current (NC) and Charged Current (CC) processes. Fig. 15 shows the differential cross section $d\sigma/dQ^2$ for both $e^{\pm}p$ NC and CC reactions [2]. The effect of W/Z exchange in the cross sections at high Q^2 is clearly visible. The Standard Model (SM) shows good agreement with the data over 6 orders of magnitude. Thus, QCD and EW effects completely explain the data. Unification of the EW forces is also clearly visible.

Fig. 16 shows the comparison [2] of the e^+p and e^-p reduced cross sections. The differences are understood as being due to the interference of the photon and Z exchange contributions, since e^-p contains constructive interference while e^+p exhibits destructive $\gamma - Z$ interference. The difference between the two reduced cross sections can be used to determine the

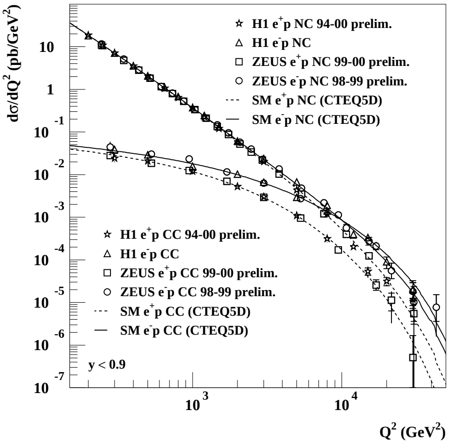

Fig. 15. Comparison of the H1 and ZEUS data for $e^{\pm}p$ neutral and charged current cross sections as a function of Q^2. The curves are the Standard Model expectations using the CTEQ5D parton distributions.

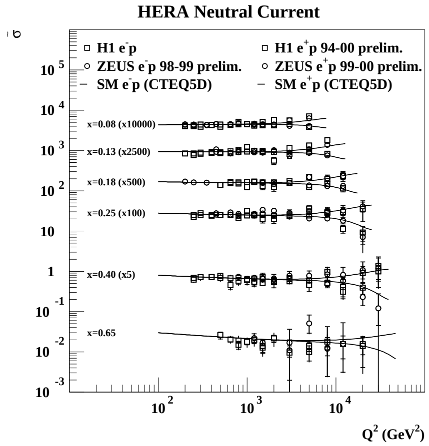

Fig. 16. A comparison of the reduced cross sections for neutral current $e^{\pm}p$ scattering as a function of Q^2 at fixed x.

quantity xF_3. The result [2] is shown in Fig. 17, where the difference in the $\sqrt{s}$ values for $e^{\pm}p$ data has been taken into account:

$$\tilde{\sigma}^{-}_{\mathrm{NC}} - \tilde{\sigma}^{+}_{\mathrm{NC}} = xF_3 \left[\frac{Y_{-920}}{Y_{+920}} + \frac{Y_{-820}}{Y_{+820}} \right] . \tag{6}$$

The results are consistent with the expectations of the SM but have limited statistical precision. Clearly, more $e^{-}p$ data are needed during the HERA-II running period.

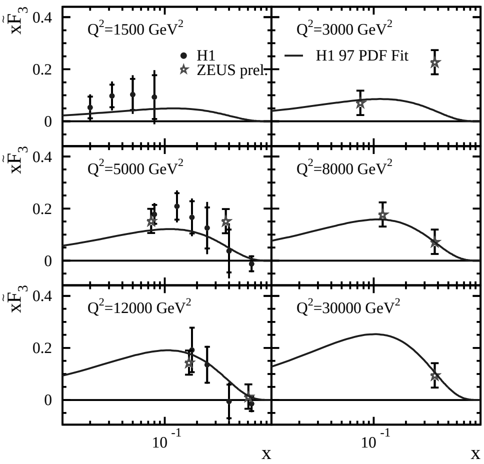

Fig. 17. A comparison of the xF_3 values obtained by H1 and ZEUS as a function of x at fixed Q^2.

These cross sections are also sensitive to the individual quark flavors. The reduced cross sections can be approximated by

$$\tilde{\sigma}_{\mathrm{CC}} \approx x\,,[\bar{u}+\bar{c}+(1-y)^2(d+s)] \tag{7}$$

and

$$\tilde{\sigma}_{\mathrm{CC}} \approx x\,,[u+c+(1-y)^2(\bar{d}+\bar{s})] \tag{8}$$

for e^+p and e^-p, respectively. The e^+p CC cross sections are shown in Fig. 18

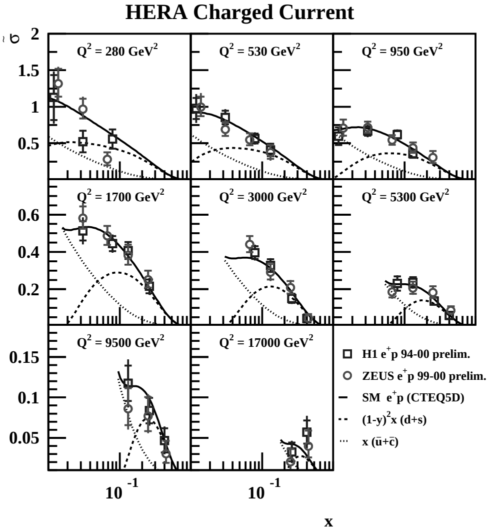

Fig. 18. A comparison of the reduced charged current cross sections from H1 and ZEUS. The lines show SM expectations for the parton distributions from CTEQ5D.

as a function of x at fixed Q^2 [2]. The NLO fits give a good description of these data. The ZEUS CC data for $e^{\pm}p$ are shown in Fig. 19 as a function of $(1-y)^2$ [7]. The intercept at $(1-y)^2 = 0$ for the e^-p data yields u_v, while the slope of the e^+p data yields d_v. Again, the measurements are well described by the PDFs from the NLO fits.

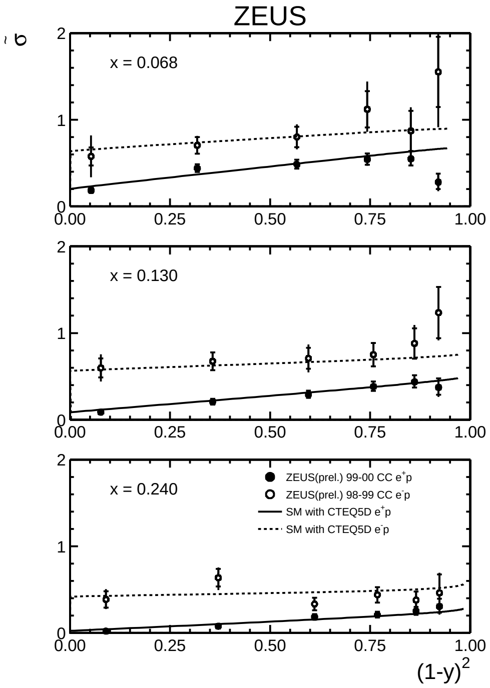

Fig. 19. The reduced cross section as a function of $(1-y)^2$ for different bins in x, for e^+p (solid dots) and e^-p (open dots). The points represent the data, while the Standard Model evaluated using the CTEQ5D PDFs are shown as the dashed and solid lines.

3. Measurements of the photon structure function, F_2^{γ}

The structure of the photon is investigated by the DIS of a virtual photon on a quasi-real photon at LEP. The kinematic region studied is shown in Fig. 20 [8] which also displays the region attainable at HERA through studies of jet production in photoproduction. At HERA, photoproduction can occur at Leading Order (LO) via either the "direct" process, Photon–Gluon Fusion (PGF) Fig. 21(a), or a "resolved" process, as shown in Fig. 21(b)–(d).

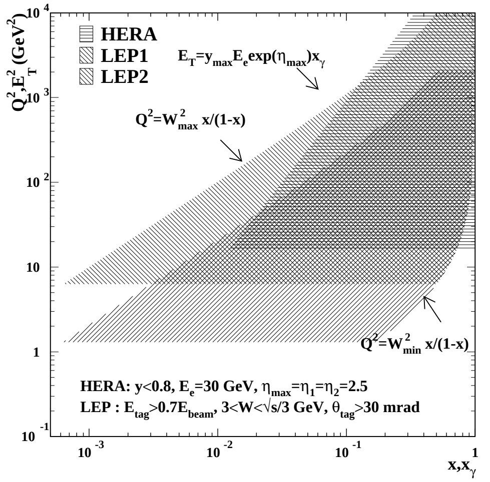

Fig. 20. Accessible kinematic plane in (Q^2, x) for HERA, LEP1 and LEP2.

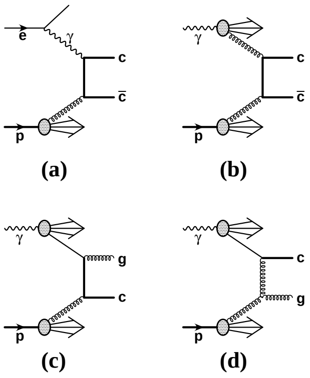

Fig. 21. Various diagrams for dijet photoproduction. (a) corresponds to the leading order direct process (photon-gluon-fusion), (b)–(d) correspond to LO resolved diagrams.

3.1. Scaling violations in F_2^γ

Fig. 22 [9] demonstrates positive scaling violations as a function of Q^2 for all x. This is in contrast to the situation observed for the proton where the positive scaling violations observed at low x turn into negative scaling violations at large x, see Fig. 4. The data are in agreement with the QCD expectations based on the various photon PDFs. Fig. 23 [9] displays F_2^γ/α as a function of x, at fixed Q^2. At the present time, the data are inconclusive concerning a possible rise at low x, as observed for the proton. The photon PDFs describe the data at the 10–20% level.

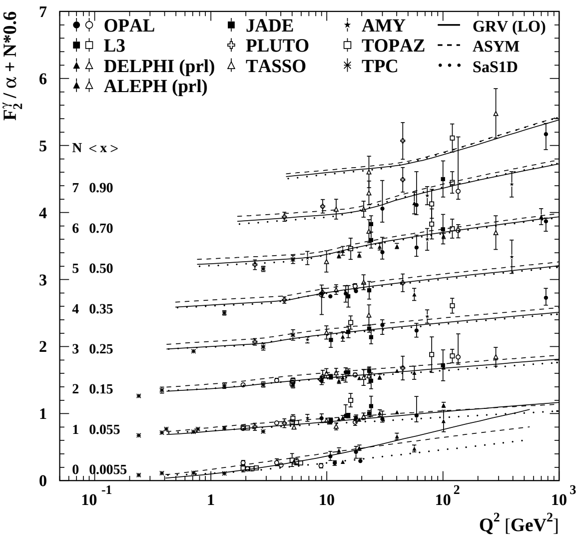

Fig. 22. Measurements of the hadronic structure function F_2^γ/α from LEP as a function of Q^2 at fixed values of x.

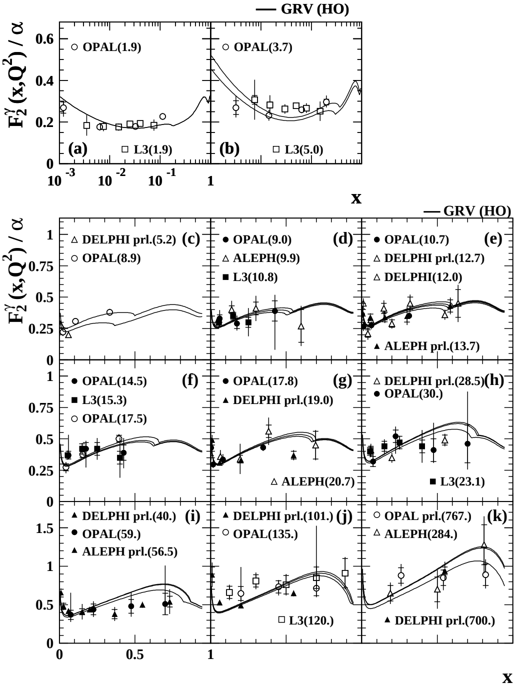

Fig. 23. Measurements of the hadronic structure function F_2^γ/α from LEP as a function of x at fixed values of Q^2.

3.2. Photon structure from HERA

The dijet cross section as a function of the dijet scattering angle, $|\cos\theta^*|$, is shown in Fig. 24 [10]. The angle, θ^*, is defined as the angle between the jet–jet axis and the beam in the dijet rest frame

$$\cos\theta^* = \tanh\left[\frac{(\eta_1 - \eta_2)}{2}\right], \tag{9}$$

where $\eta_{1,2}$ are the pseudorapidities of the two jets. The data are shown separately for $x_\gamma^{\rm obs} < 0.75$, Fig 24(a), and for $x_\gamma^{\rm obs} > 0.75$, Fig 24(b). The variable $x_\gamma^{\rm obs}$ is defined as

$$x_\gamma^{\rm obs} = \frac{E_{\rm T}^{\rm jet1} e^{-\eta_1} + E_{\rm T}^{\rm jet2} e^{-\eta_2}}{2yE_e}\,. \tag{10}$$

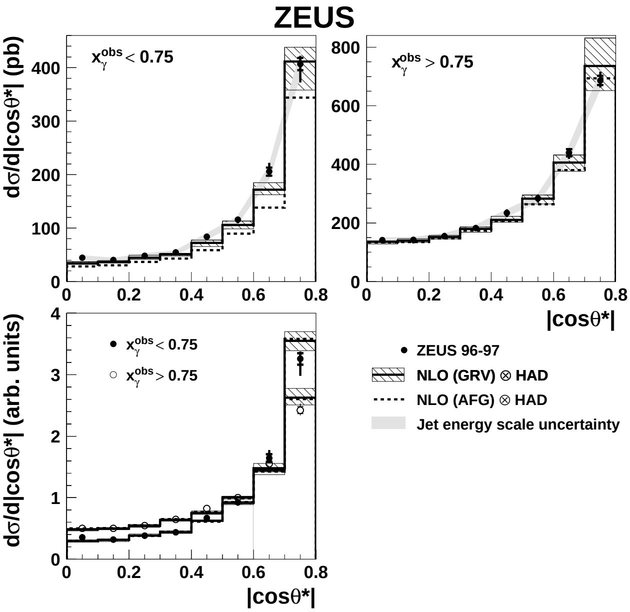

Fig. 24. Measured cross sections as a function of $|\cos\theta^*|$ for (a) $x_\gamma^{\rm obs} < 0.75$ and (b) $x_\gamma^{\rm obs} > 0.75$, compared to NLO calculations. In (c), the cross sections are area-normalized and the data shown for $x_\gamma^{\rm obs} < 0.75$ (solid points) and for $x_\gamma^{\rm obs} > 0.75$ (open points).

The data are compared to NLO predictions using either the GRV or AFG PDFs for the photon and CTEQ5M1 for the proton. The quark propagator in Fig. 21(a)–(c) yields a $(1-|\cos\theta^*|)^{-1}$ dependence while the gluon propagator of Fig. 21(d) yields a $(1-|\cos\theta^*|)^{-2}$ dependence. The data are in agreement with the expected dominance of the resolved contribution for $x_\gamma^{\rm obs} < 0.75$ in Fig. 24(a). The agreement in shape of these distributions, which are sensitive to the matrix elements, demonstrates that the dynamics of the short-distance parton-parton scattering process is well understood.

3.3. H1 and ZEUS comparison

The H1 and ZEUS data are compared [11] as a function of the $E_{\rm T}$ of the jet in Fig. 25 and are seen to be in excellent agreement. Similarly, the data are compared in Fig. 26 as a function of the pseudorapidity of the jet, $\eta^{\rm jet}$, for two different minimum values of $E_{\rm T}^{\rm jet}$ [11]. Again the data are in agreement.

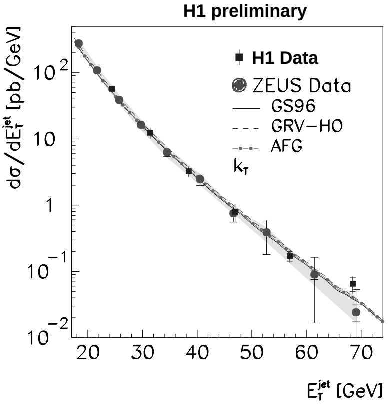

Fig. 25. A comparison of the differential e^+p cross section for inclusive jet production from H1 and ZEUS in the same kinematic region.

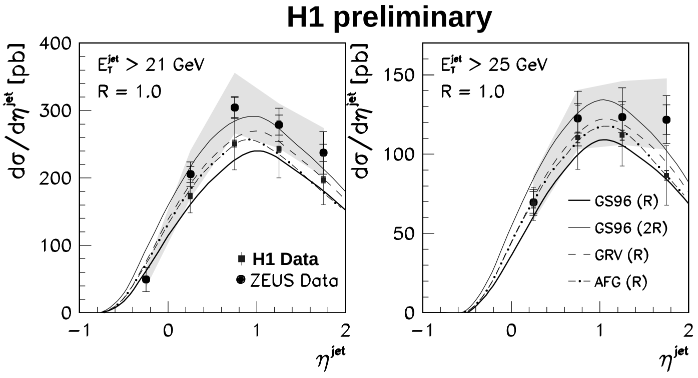

Fig. 26. A comparison of the differential e^+p cross section for inclusive jet production from H1 and ZEUS in the same kinematic region for two different thresholds in $E_{\rm T}^{\rm jet}$.

These data can be compared to NLO calculations. This has been performed by both ZEUS and H1. In Figs. 27 and 28, the ZEUS data [10] for low $x_\gamma^{\rm obs}$ lie above the NLO calculations, and more so at higher $E_{\rm T}^{\rm jet}$. This suggests that the photon PDFs are not quite correct.

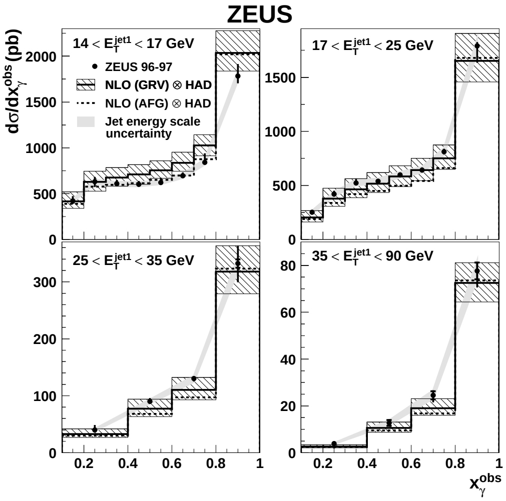

Fig. 27. Measured cross section from ZEUS as a function of $x_\gamma^{\rm obs}$ in four regions of $E_{\rm T}^{\rm jet1}$ compared to NLO predictions.

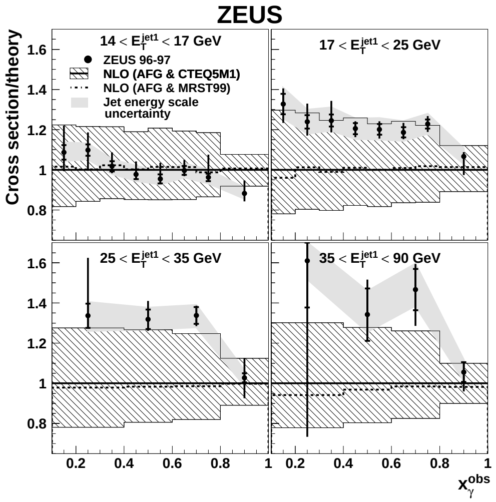

Fig. 28. Ratio of the cross sections in Fig. 27 to the NLO prediction using the GRV-HO and CTEQ5M1 PDFs. Predictions using MRST99 are also shown.

However, Figs. 29 and 30 show the H1 data [12] and indicate that the NLO description is in good agreement. This suggests that the photon PDFs are correct. A possible explanation for this apparent disagreement may be seen in Fig. 31 which shows [10] the dijet cross section for different regions in $x_\gamma^{\rm obs}$ and for $25 < E_{\rm T}^{\rm jet1} < 35$ GeV as a function of the minimum cut on the $E_{\rm T}$ of the second jet. For the kinematic cuts of the ZEUS data, $E_{\rm T}^{\rm jet2} > 11$ GeV, the data lie above the NLO, while for the cuts on the H1 data, $E_{\rm T}^{\rm jet2} > 15$ GeV, the NLO and data agree. Thus it seems that the apparent disagreement is due to the different kinematic regions being studied and not to any disagreement in the data themselves.

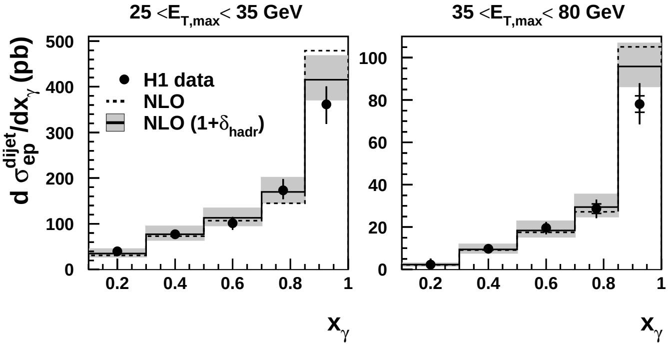

Fig. 29. Differential cross sections for H1 for dijet production for low and high $E_{\rm T}^{\rm jet}$.

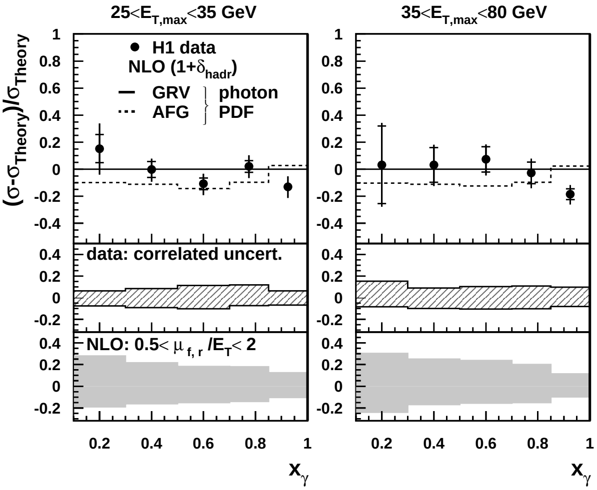

Fig. 30. Ratio of the cross sections in Fig. 29 to the NLO predictions using the GRV-HO and CTEQ5M PDFs. Also shown is the ratio using AFG-HO for the photon PDF.

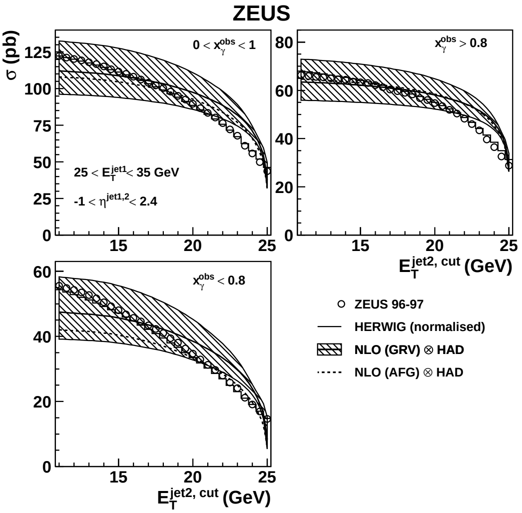

Fig. 31. Measured cross section as a function of $E_T^{\rm jet2}$ cut for $25 < E_T^{\rm jet1} < 35$ GeV compared to Monte Carlo and NLO calculations. The calculation uses CTEQ5M1 for the proton PDF and either GRV-HO or AFG-HO for the photon PDF.

3.4. Charm content in the photon

Fig. 32 shows [13] the clear production of D^* mesons in the ZEUS photoproduction data. Using these events as an indication of charm quark production, Fig. 33 shows [13] the $|\cos\theta^*|$ distribution separately for "resolved" and "direct" events. The "resolved" data sample is steeper than the "direct"

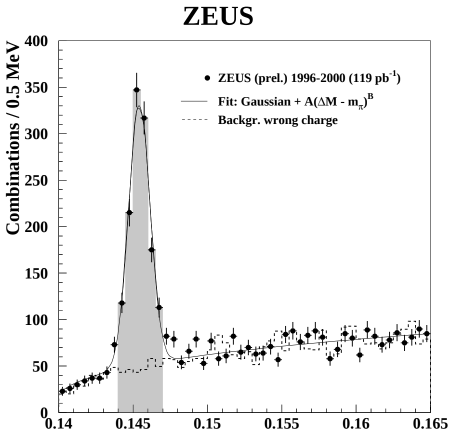

Fig. 32. The distribution of $\Delta M = M(K\pi\pi_s) - M(K\pi)$ for dijet events in the D^0 signal region (1.83–1.90 GeV).

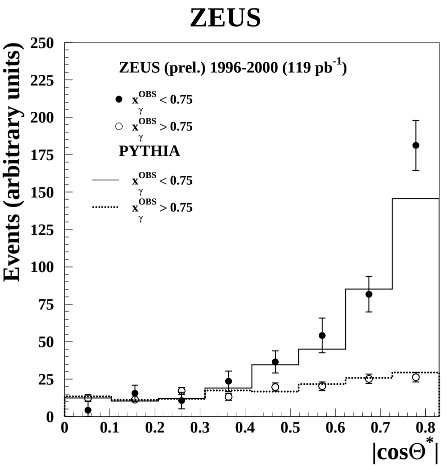

Fig. 33. Differential distributions for D^* production compared to PYTHIA. Results are given separately for direct photon (open points/dashed line) and resolved photon (black dots/full histogram) events. All distributions are normalized to the resolved data distribution in the lowest four bins.

sample, suggesting that the gluon propagator is responsible for the former. This can be understood as the dominance of the diagram in Fig. 21(d), thus suggesting a charm content in the photon. An update to this analysis may be found in Padhi's talk [14].

4. QCD measurements of α_s at HERA

Fig. 34 shows a compilation of the determinations of α_s by various methods at HERA [15]. Included are results from NLO fits to the F_2 of the proton, from the number of subjets, from jet shapes, from inclusive jet rates and from dijet rates. All of the values are in good agreement with each other and with the PDG and Bethke averages. At the present time, the precision is limited by the theoretical uncertainties.

5. Conclusions

Since DIS2001, much progress has been achieved in understanding how to incorporate the experimental uncertainties into the determination of the uncertainties in the resulting parton distribution functions. The data at high Q^2 can be used to constrain the PDFs but more data are needed from the HERA-II run. Final LEP results are providing additional information about the photon parton distributions and simultaneous fits to LEP data and HERA photoproduction data may help to determine the photon PDFs more precisely. At the moment, theoretical uncertainties limit the precision of the α_s measurements coming from HERA.

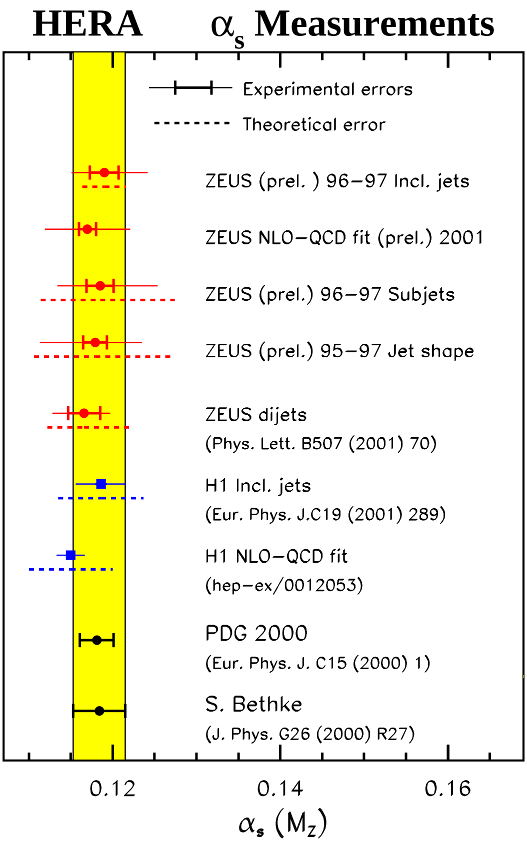

Fig. 34. Summary of α_s measurements at HERA.

REFERENCES

[1] ZEUS Collab., Paper No. 628 submitted to the EPS2001 Conference.

[2] H1 and ZEUS Collaborations, private communication. The plots may be obtained from: `http://www-zeus.desy.de/physics/sfew/PUBLIC/public.html`.

[3] C. Adloff *et al.*, (H1 Collab.), *Eur. Phys. J.* **C21**, 33 (2001).

[4] E. Tassi, not submitted to the Proceedings.

[5] B. Reisert, not submitted to the Proceedings.

[6] CTEQ6, J. Pumplin *et al.*, JHEP 0207:012 (2002); `hep-ph/0201195`.

[7] ZEUS Collab., Paper No. 631 submitted to the EPS2001 Conference.

[8] `http://opal.web.cern.ch/Opal/phys/twophoton/plots.html`.

[9] `http://www.mppmu.mpg.de/ñisius/`.

[10] S. Chekanov *et al.*, (ZEUS Collab.), *Eur. Phys. J.* **C23**, 6 (2002).

[11] S. Caron, (H1 Collab.), talk at EPS2001; H1prelim-01-132.

[12] C. Adloff *et al.*, (H1 Collab.), to be published in *Eur. Phys. J.* **C**.

[13] ZEUS Collab., Paper No. 499 submitted to the EPS2001 Conference.

[14] S. Padhi, *Acta Phys. Pol.*, **B33**, 3189 (2002).

[15] H1 and ZEUS Collaborations, private communication.